Available online at www.sciencedirect.com
ScienceDirect
Journal of Computational Physics 227 (2008) 7160–7177
JOURNAL OF COMPUTATIONAL PHYSICS
www.elsevier.com/locate/jcp

Textbook-efficiency multigrid solver for three-dimensional unsteady compressible Navier–Stokes equations

Wei Liao [a,*], Boris Diskin [b,c], Yan Peng [a], Li-Shi Luo [a]

[a] Department of Mathematics and Statistics, Center for Computational Sciences, Old Dominion University, Norfolk, VA 23529, USA
[b] National Institute of Aerospace, Hampton, VA 23666, USA
[c] Department of Mechanical and Aerospace Engineering, University of Virginia, Charlottesville, VA 22904-4746, USA

Received 21 July 2007; received in revised form 9 March 2008; accepted 17 March 2008
Available online 28 March 2008

Abstract

Implicit time-integration techniques are envisioned to be the methods of choice for direct numerical simulations (DNS) for flows at high Reynolds numbers. Therefore, the computational efficiency of implicit flow solvers becomes critically important. The textbook multigrid efficiency (TME), which is the optimal efficiency of a multigrid method, is achieved if accurate solutions of the governing equations are obtained with the total computational work that is a small (less than 10) multiple of the operation count in one residual evaluation. In this paper, we present a TME solver for unsteady subsonic compressible Navier–Stokes equations in three dimensions discretized with an implicit, second-order accurate in both space and time, unconditionally stable, and non-conservative scheme. A semi-Lagrangian approach is used to discretize the time-dependent convection part of the equations; viscous terms and the pressure gradient are discretized on a staggered grid. The TME solver for the implicit equations is applied at each time level. The computational efficiency of the solver is designed to be independent of the Reynolds number. Our tests show that the proposed solver maintains its optimal efficiency at high Reynolds numbers and for large time steps.

Keywords: Textbook-efficiency multigrid; Implicit method; Distributed relaxation; Compressible flow; Navier–Stokes equations; DNS

1. Introduction

In the realm of computational fluid dynamics (CFD), the direct numerical simulation (DNS) is one of the most important methodology to study flow physics numerically, especially for turbulence of compressible [1–8] and incompressible [9–12] flows. The DNS methodology relies on spatial discretizations of the Navier–Stokes equations with various techniques, such as finite difference, finite volume, finite element, pseudo-spectral, etc., and various time-integration techniques. With ever increasing computing resources ubiquitously available, DNS is becoming a more and more powerful means to study turbulence, combus-

* Corresponding author. Tel.: +1 757 6836001x5035; fax: +1 757 6833885.
E-mail addresses: wliao@odu.edu (W. Liao), bdiskin@nianet.org (B. Diskin), ypeng@odu.edu (Y. Peng), lluo@odu.edu (L.-S. Luo).

0021-9991/$ - see front matter © 2008 Elsevier Inc. All rights reserved.
doi:10.1016/j.jcp.2008.03.026

tion, and other flow phenomena. It is well known that the $Re^{9/4}$ degrees of freedom are required for a DNS to resolve a flow of Reynolds number Re [13]. Thus, for example, to simulate a turbulent flow at $Re = O(10^5)$, a resolution of $N^3 = O(10^{11})$ is required. In addition to sufficient spatial resolution determined by the Reynolds number, appropriate time resolution must also be considered. Kolmogorov's universal equilibrium theory postulates that the fundamental spatial and temporal scales of turbulence are the Kolmogorov length scale $l := (v^3/\langle\varepsilon\rangle)^{1/4}$ and time scale $\tau := (v/\langle\varepsilon\rangle)^{1/2}$, respectively, where v is the kinematic viscosity and $\langle\varepsilon\rangle$ is the mean dissipation rate [13]. For explicit time-stepping schemes, the Courant–Freidricks–Levy (CFL) number criterion,

$$\mathrm{CFL} = \frac{h_t c_s (Ma + 1)}{h_x} \leqslant 1, \tag{1}$$

limits the time step size h_t; here c_s is the speed of sound, Ma is the Mach number, and h_x is the grid spacing. In CFD computations, the CFL number computed according to (1) is sometimes referred as acoustic CFL number to distinguish it from convective $\mathrm{CFL_c}$ number computed as

$$\mathrm{CFL_c} = \frac{h_t c_s Ma}{h_x}. \tag{2}$$

In explicit schemes for turbulent flows, the maximal time step h_t is determined by l/U, where U is the characteristic velocity of energy containing eddies. It can be shown that $h_t/\tau = O(Re^{-1/4})$ [13], implying that, for high Reynolds number flows, the time step h_t allowed by the CFL criterion is far smaller than the Kolmogorov time scale τ. In this scenario, $\tau \gg h_t$, explicit time-integration techniques are no longer efficient computationally. To circumvent the limitation of $\mathrm{CFL} \leqslant 1$, implicit time-integration schemes must be considered.

Multigrid methods have been generally accepted as the fastest solution techniques for elliptic and other types of partial differential equations (PDEs) and have been successfully used for many CFD applications; numerous references can be found in various textbooks (e.g., [14]). To compare efficiency of various solvers, Brandt introduced the notion of a minimal work unit [15], which is defined as the computational work involved in one residual evaluation. An optimal multigrid method demonstrating the textbook multigrid efficiency (TME) obtains the solutions of the system of governing equations in a total computational work of less than 10 minimal work units [15,16]. Several publications review methodologies for achieving TME in CFD applications [15,17–20]. Brandt [21] compiled a comprehensive list of TME demonstrations, pointed out existing barriers for extending TME to further CFD applications, and suggested ways to overcome these barriers.

The basic framework for nonlinear TME solvers resides in full multigrid (FMG) algorithms [14,15,22,23]. In FMG algorithms, the solution process starts on a coarse-grid, on which the computational cost to obtain an accurate solution is insignificant. This coarse-grid solution is then interpolated to the next finer grid as an initial approximation. A very few multigrid full approximation scheme (FAS) cycles, or just one, are required to obtain an accurate solution on the finer grid. This process continues until the solution on the targeted finest grid is achieved.

The objective of FMG algorithms, and TME methods in particular, is to achieve an accurate approximation to the solution of the differential equations. An approximation is considered accurate if its algebraic error is smaller than the discretization error. The algebraic error is defined as the difference between the exact and approximate solutions of the discrete problem, while the discretization error is the difference between the exact solutions of discrete and differential problems. The latter can be accurately estimated by comparing solutions at different levels of the FMG algorithm.

In this paper, we overcome one of the most formidable barriers formulated in [21], namely, extending TME to solutions of three-dimensional (3D) unsteady compressible Navier–Stokes equations at arbitrary Reynolds numbers. The main contribution of this paper is a novel methodology that combines distributed relaxation multigrid [20,24,25] with semi-Lagrangian fully implicit discretization of time-dependent convection terms and leads to TME solvers for turbulent flows at arbitrary Reynolds number. The considered non-conservative formulation involves staggered-grid spatial discretizations for viscous terms and pressure gradient. The scheme is second-order accurate in both space and time and unconditionally stable. The multigrid solver is applied at each time level.

The proposed methodology takes advantage of a semi-Lagrangian discretization of the time-dependent convection terms, which dramatically simplifies the interior relaxation scheme. The main benefits of the semi-Lagrangian discretization include (i) eliminating closed convection characteristics that represent a major difficulty for steady-state multigrid solutions; (ii) reducing the convection term contributions to the implicit current-time-level equations to source-like contributions, which improves ellipticity of these equations; (iii) enabling an efficient distributed relaxation that capitalizes on efficient algorithms previously developed and validated for elliptic operators; and (iv) ultimately leading to TME for unsteady compressible Navier–Stokes equations. A distinctive feature of the developed multigrid solver is that its efficiency does not deteriorate at high Reynolds numbers and at high CFL numbers. The current implementation of the multigrid solver is serial, but all solver components are completely local, scalable, and suitable for efficient parallel computing; good practices for efficient parallel implementation of multigrid algorithms are discussed in [19]. Thus, the proposed methodology is attractive for large-scale turbulent flow computations of practical interest. While for the reported solver (solving a non-conservative discretization on periodic domains), the applications are limited to smooth subsonic interior flows with no boundaries, extensions to flows with general boundary conditions and, probably, to conservative formulations suitable for discontinuous flows are possible and currently researched.

The paper is organized as follows. In Section 2 we describe briefly the compressible Navier–Stokes equations and related transport coefficients. In Section 3 we discuss the discrete formulation for the compressible Navier–Stoke equations in 3D. Numerical studies of accuracy of this discrete formulation are reported in Section 4. In Section 5, we introduce the multigrid solver used in this work. In particular, we discuss components of the outer nonlinear multigrid cycle and, specifically, an efficient distributed relaxation procedure that involves inner multigrid. In Section 6 we present our numerical results. We first present a series of tests demonstrating the optimal convergence rates of the residual and the algebraic errors. We also confirm TME by demonstrating accurate solutions that obtained in less than 10 minimal work units. The TME solver is also applied for DNS of decaying homogeneous isotropic turbulence in 3D. Finally, in Section 7, we summarize our work and discuss future research directions. We also provide three appendices. Linear stability of a one-dimensional semi-Lagrangian discretization is shown in Appendix A. Appendix B shows the details of the inter-grid transfers used by the outer multigrid cycle, and Appendix C provides a local mode Fourier (LMF) analysis explaining the generation of spurious high-frequency errors in red–black relaxation.

2. Fully compressible Navier–Stokes equations in 3D

The system of time-dependent compressible Navier–Stokes equations can be written as

$$\partial_t \mathbf{Q} + \mathbf{R} = \bar{\mathbf{f}}, \tag{3}$$

where $\mathbf{Q} := (\rho u, \rho v, \rho w, \rho, \rho E)^{\mathsf{T}}$ is the vector of conserved variables, whose components are the momentum $\rho \boldsymbol{u} := (\rho u, \rho v, \rho w)$, the density ρ, and the specific total energy ρE, $\bar{\mathbf{f}}$ is the vector of sourcing terms, and $\mathbf{R}$ is the gradient of the fluxes:

$$\mathbf{R} := \partial_x \mathbf{F}_x + \partial_y \mathbf{F}_y + \partial_z \mathbf{F}_z, \tag{4}$$

where $\mathbf{F}_\alpha := (\Pi_{\alpha x}, \Pi_{\alpha y}, \Pi_{\alpha z}, \rho u_\alpha, K_\alpha)^{\mathsf{T}}$,

$$\Pi_{\alpha\beta} := \rho u_\alpha u_\beta - \sigma_{\alpha\beta} := \rho u_\alpha u_\beta + p\delta_{\alpha\beta} - \tau_{\alpha\beta}, \tag{5a}$$

$$\tau_{\alpha\beta} := \mu\left(\partial_\alpha u_\beta + \partial_\beta u_\alpha - \frac{2}{3}(\nabla \cdot \boldsymbol{u})\delta_{\alpha\beta}\right) + \zeta(\nabla \cdot \boldsymbol{u})\delta_{\alpha\beta}, \tag{5b}$$

$$\boldsymbol{K} := \rho E \boldsymbol{u} + \mathsf{P} \cdot \boldsymbol{u} + \boldsymbol{H}, \quad \boldsymbol{H} := -\kappa \nabla \epsilon, \tag{5c}$$

$\alpha, \beta \in \{x, y, z\} := \{1, 2, 3\}$, μ and ζ are the dynamic and bulk viscosities, respectively, κ is the heat conductivity, ϵ is the specific internal energy, and p is the pressure; $\Pi_{\alpha\beta}$, $\sigma_{\alpha\beta}$ and $\tau_{\alpha\beta}$ are the momentum flux tensor, the stress tensor and the shear stress tensor, respectively, and E and $\boldsymbol{H}$ are the total energy flux and the heat flux, respectively. The fluxes can be written out explicitly as the following:

$$\mathbf{F}_x = \begin{pmatrix} \rho uu + p - 2\mu\partial_x u - \lambda\nabla\cdot\boldsymbol{u} \\ \rho vu - \mu(\partial_x v + \partial_y u) \\ \rho wu - \mu(\partial_x w + \partial_z u) \\ \rho u \\ (\rho E + p)u - u_\alpha\tau_{\alpha x} - \kappa\partial_x\epsilon \end{pmatrix}, \tag{6a}$$

$$\mathbf{F}_y = \begin{pmatrix} \rho uv - \mu(\partial_x v + \partial_y u) \\ \rho vv + p - 2\mu\partial_y v - \lambda\nabla\cdot\boldsymbol{u} \\ \rho wv - \mu(\partial_y w + \partial_z v) \\ \rho v \\ (\rho E + p)v - u_\alpha\tau_{\alpha y} - \kappa\partial_y\epsilon \end{pmatrix}, \tag{6b}$$

$$\mathbf{F}_z = \begin{pmatrix} \rho uw - \mu(\partial_x w + \partial_z u) \\ \rho vw - \mu(\partial_y w + \partial_z v) \\ \rho ww + p - 2\mu\partial_z w - \lambda\nabla\cdot\boldsymbol{u} \\ \rho w \\ (\rho E + p)w - u_\alpha\tau_{\alpha z} - \kappa\partial_z\epsilon \end{pmatrix}, \tag{6c}$$

where $\lambda := \zeta - \frac{2}{3}\mu$ and the Einstein notation of summation over repeated indexes is used, thus,

$$u_\alpha\tau_{\alpha x} = \mu[2u\partial_x u + v(\partial_x v + \partial_y u) + w(\partial_x w + \partial_z u)] + \lambda u\nabla\cdot\boldsymbol{u}, \tag{7a}$$

$$u_\alpha\tau_{\alpha y} = \mu[2v\partial_y v + w(\partial_y w + \partial_z v) + u(\partial_x v + \partial_y u)] + \lambda v\nabla\cdot\boldsymbol{u}, \tag{7b}$$

$$u_\alpha\tau_{\alpha z} = \mu[2w\partial_z w + u(\partial_x w + \partial_z u) + v(\partial_y w + \partial_z v)] + \lambda w\nabla\cdot\boldsymbol{u}. \tag{7c}$$

In general, the simplest form of the Navier–Stokes equations is a non-conservative formulation expressed in terms of primitive variables, $\mathbf{q} = (u, v, w, p, \epsilon)^{\mathsf{T}}$, where $\boldsymbol{u} := (u, v, w)$ is the flow velocity vector, p is the pressure, and ϵ is the internal energy. For a perfect gas, the primitive variables are connected through the following relations

$$p = (\gamma - 1)\rho\epsilon, \tag{8a}$$

$$\epsilon = E - \frac{1}{2}\left(u^2 + v^2 + w^2\right), \tag{8b}$$

$$c_s^2 = \gamma p/\rho, \tag{8c}$$

where c_s is the speed of sound and γ is the ratio of specific heats, taken here as $\gamma = 1.4$.

The time-dependent non-conservative equations are found readily by transforming the time-dependent conservative equations

$$\begin{aligned} &\frac{\partial\mathbf{q}}{\partial\mathbf{Q}}[\partial_t\mathbf{Q} + \mathbf{R}] = \frac{\partial\mathbf{q}}{\partial\mathbf{Q}}\bar{\mathbf{f}}, \\ &\partial_t\mathbf{q} + \frac{\partial\mathbf{q}}{\partial\mathbf{Q}}\mathbf{R} = \hat{\mathbf{f}}, \end{aligned} \tag{9}$$

where $\frac{\partial\mathbf{q}}{\partial\mathbf{Q}}$ is the Jacobian matrix of the transformation and $\hat{\mathbf{f}} = (\hat{f}_u, \hat{f}_v, \hat{f}_w, \hat{f}_p, \hat{f}_\epsilon)^{\mathsf{T}}$. The resulting set of equations is [1]

$$\mathcal{D}_t u + \left(-\frac{\mu}{\rho}\Delta - \frac{\hat{\lambda}}{\rho}\partial_{xx}\right)u - \frac{\hat{\lambda}}{\rho}(\partial_{xy}v + \partial_{xz}w) + \frac{1}{\rho}\partial_x p = \hat{f}_u, \tag{10a}$$

[1] Eqs. (10d) and (10e) correct some typos appeared in the previous papers [17,18]. Specifically, the sign of the terms of Φ is changed and the term of Φ/ρ in (10e) replaces $\rho\Phi$.

$$\mathcal{D}_t v + \left(-\frac{\mu}{\rho}\Delta - \frac{\hat{\lambda}}{\rho}\partial_{yy}\right)v - \frac{\hat{\lambda}}{\rho}(\partial_{xy}u + \partial_{yz}w) + \frac{1}{\rho}\partial_y p = \hat{f}_v, \tag{10b}$$

$$\mathcal{D}_t w + \left(-\frac{\mu}{\rho}\Delta - \frac{\hat{\lambda}}{\rho}\partial_{zz}\right)w - \frac{\hat{\lambda}}{\rho}(\partial_{xz}u + \partial_{yz}v) + \frac{1}{\rho}\partial_z p = \hat{f}_w, \tag{10c}$$

$$\mathcal{D}_t p + \rho c_s^2(\nabla\cdot\boldsymbol{u}) - (\gamma-1)(\kappa\Delta\epsilon + \Phi) = \hat{f}_p, \tag{10d}$$

$$\mathcal{D}_t \epsilon + \frac{c_s^2}{\gamma}(\nabla\cdot\boldsymbol{u}) - \frac{\kappa}{\rho}\Delta\epsilon - \frac{1}{\rho}\Phi = \hat{f}_\epsilon, \tag{10e}$$

where the dissipation function Φ is defined by

$$\begin{aligned}\Phi &\equiv \tau_{\alpha\beta}\partial_\alpha u_\beta \\ &= \mu[2(\partial_x u)^2 + 2(\partial_y v)^2 + 2(\partial_z w)^2 + (\partial_x v + \partial_y u)^2 + (\partial_x w + \partial_z u) + (\partial_y w + \partial_z v)^2] + \lambda(\partial_x u + \partial_y v \\ &\quad + \partial_z w)^2,\end{aligned} \tag{11}$$

$\mathcal{D}_t \equiv \partial_t + (\boldsymbol{u}\cdot\nabla)$ is a nonlinear time-dependent convection operator and $\hat{\lambda} = \lambda + \mu$. According to the Stokes hypothesis, $\zeta = 0$ and $\lambda = -2/3\mu$, then $\hat{\lambda} = \mu/3$. In what follows, the first three equations are referenced as momentum equations, the fourth and fifth equations are called the pressure and the energy equations, respectively. Eqs. (10) are defined on a periodic domain and are subject to initial conditions generally considered as a collection of vortexes. The flows are assumed subsonic implying

$$0 \leqslant \sqrt{u^2 + v^2 + w^2} < c_s. \tag{12}$$

There are no restrictions on the flow Reynolds number.

3. Discrete formulation

Eqs. (10) are discretized with a second-order accurate time-implicit discretization on a uniform Cartesian grid with staggered placement of unknowns (u, v, w, p, ϵ):

$$\mathcal{D}_t^h u + \frac{1}{\bar{\rho}}[(-\mu\Delta^h - \hat{\lambda}\partial_{xx}^h)u - \hat{\lambda}(\partial_{xy}^h v + \partial_{xz}^h w) + \partial_x^h p] = \hat{f}_u^h, \tag{13a}$$

$$\mathcal{D}_t^h v + \frac{1}{\bar{\rho}}[(-\mu\Delta^h - \hat{\lambda}\partial_{yy}^h)v - \hat{\lambda}(\partial_{xy}^h u + \partial_{yz}^h w) + \partial_y^h p] = \hat{f}_v^h, \tag{13b}$$

$$\mathcal{D}_t^h w + \frac{1}{\bar{\rho}}[(-\mu\Delta^h - \hat{\lambda}\partial_{zz}^h)w - \hat{\lambda}(\partial_{xz}^h u + \partial_{yz}^h v) + \partial_z^h p] = \hat{f}_w^h, \tag{13c}$$

$$\mathcal{D}_t^h p + \rho c_s^2(\nabla^h\cdot\boldsymbol{u}) - (\gamma-1)(\kappa\Delta^h\epsilon + \Phi^h) = \hat{f}_p^h, \tag{13d}$$

$$\mathcal{D}_t^h \epsilon + \frac{c_s^2}{\gamma}(\nabla^h\cdot\boldsymbol{u}) - \frac{\kappa}{\rho}\Delta^h\epsilon - \frac{1}{\rho}\Phi^h = \hat{f}_\epsilon^h, \tag{13e}$$

where

$$\begin{aligned}\Phi^h &\equiv \mu[2(\partial_x^h u)^2 + 2(\partial_y^h v)^2 + 2(\partial_z^h w)^2 + (\partial_x^{2h} v + \partial_y^{2h} u)^2 + (\partial_x^{2h} w + \partial_z^{2h} u)^2 + (\partial_y^{2h} w + \partial_z^{2h} v)^2] \\ &\quad + \lambda(\partial_x^h u + \partial_y^h v + \partial_z^h w)^2.\end{aligned} \tag{14}$$

The arrangement of discrete variables is illustrated in Fig. 1. On a cubic cell with the edges formed by the spatial mesh, the velocity components are located on the faces normal to the corresponding directions (e.g., u is placed in the centers of faces normal to the x-direction); the pressure p and the internal energy ϵ are placed at the cell center. The discrete momentum equations are centered at the locations of the corresponding velocity components; and the pressure and energy equations are centered at the locations of the pressure. $\hat{\mathbf{f}}^h = (\hat{f}_u^h, \hat{f}_v^h, \hat{f}_w^h, \hat{f}_p^h, \hat{f}_\epsilon^h)^\mathsf{T}$ are discrete representations of sources. Values of ρ and c_s^2 are computed at the cell centers through (8). The values of $\bar{\rho}$ in

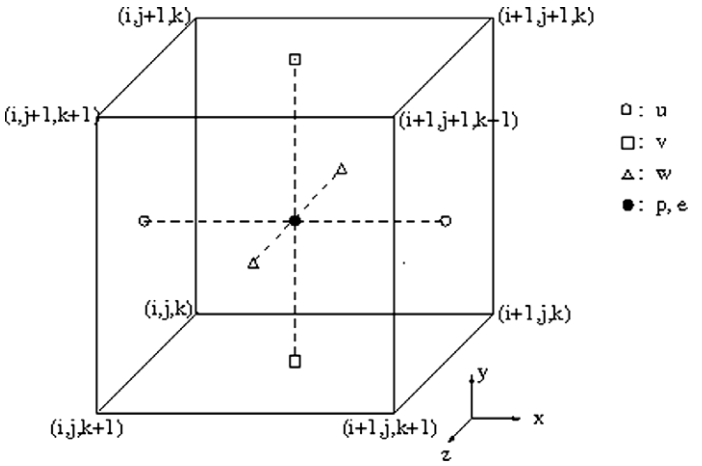

Fig. 1. Staggered arrangement of discrete variables.

the momentum equations are computed from the values of p and ϵ interpolated from the two adjacent cell centers, where the pressure and the energy are defined. The discrete derivatives ∂_x^h, ∂_y^h, and ∂_z^h are approximated as short central two-point differences; the derivatives ∂_x^{2h}, ∂_y^{2h}, and ∂_z^{2h} are approximated with four-point stencils that are derived as averages of two wide central differences; Δ^h is a standard 3D seven-point approximation to the Laplacian; the second derivatives ∂_{xx}^h, ∂_{yy}^h, and ∂_{zz}^h are approximated by three-point stencils; the mixed derivatives ∂_{xy}^h, ∂_{xz}^h, and ∂_{yz}^h are approximated by short central four-point stencils; $\mathcal{D}_t^h$ is the time-dependent convection operator discretized by a second-order semi-Lagrangian method [26].

The semi-Lagrangian discretization is performed along the convection trajectory arriving to the given grid point at the current-time-level. For the second-order accuracy, the trajectory is assumed to be a straight line with the direction defined by the local velocity vector at the arrival point. The trajectory is traced two time steps backward. A one-dimensional illustration of the semi-Lagrangian discretization is shown in Fig. 2. The solution values at the previous-time-levels are linearly interpolated (in 3D, from the eight surrounding nodes) to the departure and transition points and weighted to ensure the second-order accurate stable approximation for the operator $\mathcal{D}_t$

$$\mathcal{D}_t^h p_{i_x,i_y,i_z}^n \equiv \frac{1}{2h_t}\left(3p_{i_x,i_y,i_z}^n - 4\sum_{i,j,k=0}^{1}\frac{s_x^i}{(1-s_x)^{i-1}}\frac{s_y^j}{(1-s_y)^{j-1}}\frac{s_z^k}{(1-s_z)^{k-1}}p_{i_x-(k_x+i),i_y-(k_y+j),i_z-(k_z+k)}^{(n-1)} + \sum_{i,j,k=0}^{1}\frac{s_x^i}{(1-s_x)^{i-1}}\frac{s_y^j}{(1-s_y)^{j-1}}\frac{s_z^k}{(1-s_z)^{k-1}}p_{i_x-2(k_x+i),i_y-2(k_y+j),i_z-2(k_z+k)}^{(n-2)}\right), \tag{15}$$

where, for the given point velocity vector $(u,v,w)_{i_x,i_y,i_z}^n$, $u_{i_x,i_y,i_z}^n h_t = (k_x + s_x)h_x$, k_x is an integer and $0 \leqslant s_x < 1$; analogously, $v_{i_x,i_y,i_z}^n h_t = (k_y + s_y)h_y$ and $w_{i_x,i_y,i_z}^n h_t = (k_z + s_z)h_z$. The first differential approximation (FDA) for the operator $\mathcal{D}_t^h$ computed by the Taylor expansion in four (time and space) dimensions is given by

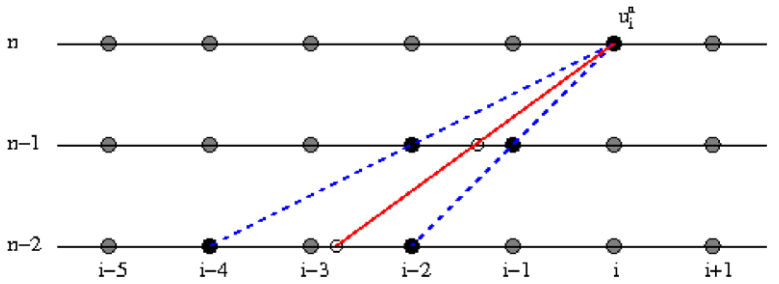

Fig. 2. Second-order accurate semi-Lagrangian discretization of the one-dimensional convection operator $\partial_t + u\partial_x$. Empty circles denote the departure and transition points; dark circles denote interpolation points.

$$\mathrm{FDA}(\mathcal{D}_t^h) = \partial_t + u\partial_x + v\partial_y + w\partial_z - \frac{h_t^2}{3}(\partial_t + u\partial_x + v\partial_y + w\partial_z)^3 - \frac{1}{3h_t}(s_x(1-s_x)(1-2s_x)h_x^3(\partial_x)^3 + s_y(1-s_y)(1-2s_y)h_y^3(\partial_y)^3 + s_z(1-s_z)(1-2s_z)h_z^3(\partial_z)^3), \tag{16}$$

confirming the second-order approximation in space and time. As a result of this discretization, the discrete convection operator makes a single-point contribution to the stencil of the implicit current-time-level equations, positively affecting the stability (diagonal dominance) of the system. In the course of this paper, we assume that the spatial grid is isotropic, i.e., has the same mesh size, $h_x = h_y = h_z = h$, in all directions; the fixed time step, h_t, is allowed to be much larger, $h_t \gg h$. The specific values of h and h_t are governed by the required resolution accuracy, not by numerical stability considerations.

4. Numerical study of discretization accuracy

The accuracy of the discretization scheme has been studied for a manufactured analytical solution of the differential equations (10) in a form resembling a traveling cylindrical vortex. For the test problem, the viscosity coefficient and thermal conductivity coefficient are chosen as $\mu = 3 \times 10^{-6}$, $\kappa = 5.83 \times 10^{-6}$, respectively. A sequence of grids is defined on the computational spatial domain chosen as a cube with the edge length $L = 1$. The manufactured analytical solution is defined as

$$\begin{aligned} u &= 1 + 0.1\sin\left[\frac{2\pi}{L}(x-0.1t)\right]\cos\left[\frac{2\pi}{L}(x-0.1t)\right], \\ v &= -0.1\cos\left[\frac{2\pi}{L}(x-0.1t)\right]\sin\left[\frac{2\pi}{L}(x-0.1t)\right], \\ w &= 0, \\ p &= 2 - \frac{u^2+v^2}{2}, \\ \epsilon &= 7 \end{aligned} \tag{17}$$

and the corresponding source functions are defined by substituting this solution into (10). The speed of sound computed for the solution is approximately $c_s = 2$, which corresponds to the Mach number approaching $Ma = 0.5$.

The sequence of tested grids includes grids with 17, 33, 65, 129, and 257 points in each spatial dimension, and the time step $h_t = 4h$ for each grid. The acoustic CFL number computed according to (1) is $\mathrm{CFL} \approx 12$; the corresponding convective CFL number given by (2) is $\mathrm{CFL_c} \approx 4$. Figs. 3 and 4 demonstrate convergence of the L_1 and L_∞ norms of the truncation and discretization errors. Truncation errors are computed as residuals obtained after substituting the exact analytical solution (17) into the discrete equations (13); recall that the discretization errors are the differences between the exact analytical and discrete solutions. The norms of truncation and discretization errors are computed over the entire time/space domain. The time interval is fixed as $[0, T]$, where $T = 0.5$, so the number of time steps is doubled for each finer grid. For computing the discretization errors, the computations are initialized at the zero time from the analytical solution; at the first (next after the zeroth) time level, the discretization of the convection term is switched to the first order; at all other time levels, the second-order accurate discretization (16) is employed. The second-order convergence of the truncation and discretization errors is observed in all norms confirming the second-order accuracy in space and time.

5. Multigrid solver

The multigrid solver is applied to solve implicit equations at each time level. The initial approximation is typically obtained from the solution at the previous-time-level. An informal requirement to the quality of the initial approximation is that it would represent a good initial solution for Newton iterations. This approximation is, then, improved by performing one outer nonlinear multigrid cycle. The term "outer" is used to distin-

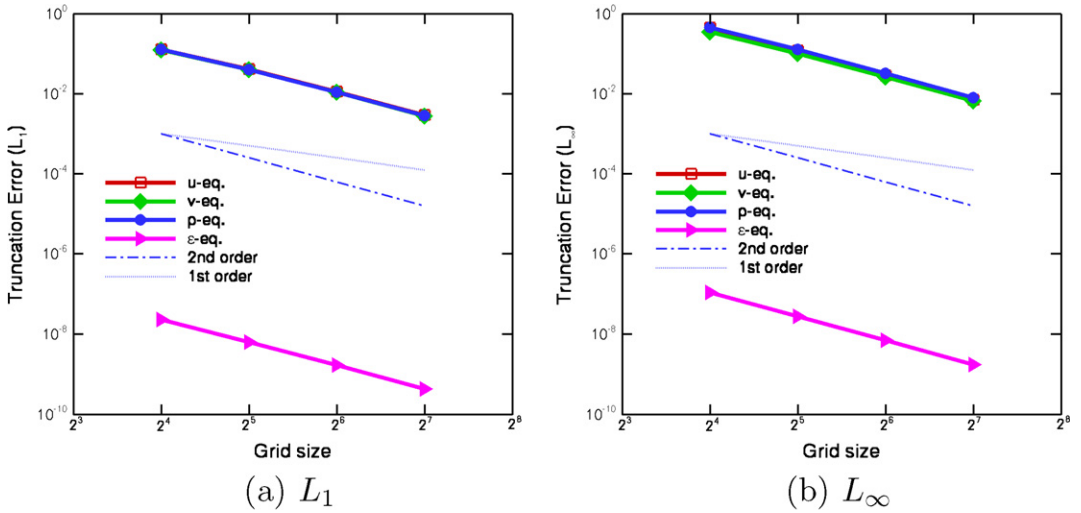

Fig. 3. L_1 and L_∞ norms of truncation errors for the discrete equations (13) and solution (17).

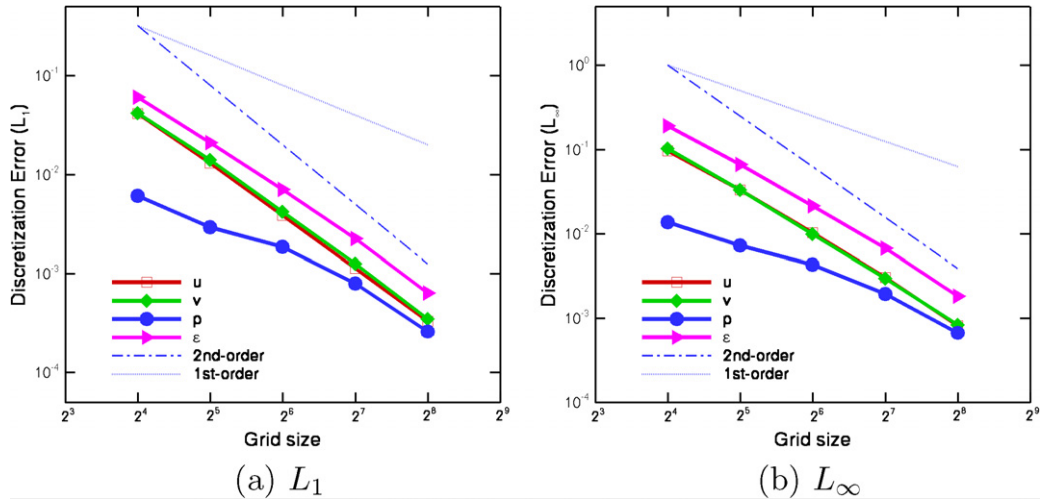

Fig. 4. L_1 and L_∞ norms of discretization errors for the solution (17).

guish the nonlinear multigrid cycle applied to the entire system of flow equations from the "inner" cycles introduced below that are applied to some linearized scalar operators and used as a part of the relaxation procedure. The implicit equations at the current-time-level are similar to (13) with the operator $\mathcal{D}_t^h$ replaced by the coefficient $\frac{3}{2h_t}$ and the discrete source function, $\mathbf{f}^h = (f_u^h, f_v^h, f_w^h, f_p^h, f_\epsilon^h)^{\mathsf{T}}$, accounting for the influence of the previous-time solutions:

$$\frac{3}{2h_t}u + \frac{1}{\bar{\rho}}[(-\mu\Delta^h - \hat{\lambda}\partial_{xx}^h)u - \hat{\lambda}(\partial_{xy}^h v + \partial_{xz}^h w) + \partial_x^h p] = f_u^h, \tag{18a}$$

$$\frac{3}{2h_t}v + \frac{1}{\bar{\rho}}[(-\mu\Delta^h - \hat{\lambda}\partial_{yy}^h)v - \hat{\lambda}(\partial_{xy}^h u + \partial_{yz}^h w) + \partial_y^h p] = f_v^h, \tag{18b}$$

$$\frac{3}{2h_t}w + \frac{1}{\bar{\rho}}[(-\mu\Delta^h - \hat{\lambda}\partial_{zz}^h)w - \hat{\lambda}(\partial_{xz}^h u + \partial_{yz}^h v) + \partial_z^h p] = f_w^h, \tag{18c}$$

$$\frac{3}{2h_t}p + \rho c_s^2(\nabla^h \cdot \boldsymbol{u}) - (\gamma - 1)(\kappa\Delta^h\epsilon + \Phi^h) = f_p^h, \tag{18d}$$

$$\frac{3}{2h_t}\epsilon + \frac{c_s^2}{\gamma}(\nabla^h \cdot \boldsymbol{u}) - \frac{\kappa}{\rho}\Delta^h\epsilon - \frac{1}{\rho}\Phi^h = f_\epsilon^h. \tag{18e}$$

In the current implementation, the trajectories used in the semi-Lagrangian approximation are computed from the initial solution approximation obtained from the previous-time-level. This approach is valid for flows with modest solution variations on the discretization time scale. To account for more volatile flows, several modifications can be suggested. First, an improved initial approximation can be obtained by shifting the local values of the previous-time-level solution along the (approximated) trajectories. Second, the trajectory used for defining the semi-Lagrangian discretization can be found as part of the solution process, not just derived from the initial guess. This approach leads to somewhat more complicated implicit equations replacing Eqs. (18). Specifically, the current-level contribution from the semi-Lagrangian operator remains one-point type (a coefficient multiplying solution component), but the coefficient becomes dependent on solutions at the previous-time-levels. The complication does not adversely affect the efficiency of the multigrid solver described below. The third possible modification can be used if the initial approximation obtained from the previous-time-level is not good enough (e.g., the Newton iterations that start from this initial approximation would not converge fast). In this case, an FMG method with continuation can be developed to improve the initial guess. However, the excellent convergence demonstrated by the current version of the algorithm for combination of large Reynolds numbers with large time steps indicates that these modifications are probably unnecessary for many practical applications.

5.1. Multigrid cycle

There are two approaches to solve nonlinear equations with multigrid. First approach employs an FAS multigrid cycle that provides approximations to the nonlinear solution on each grid involved. Another approach follows the Newton iteration recipe; it linearizes the original equations to apply linear multigrid for computing a correction to the initial solution approximation. Some comparative studies of these solution strategies and their possible combinations have been performed elsewhere [27,28]. In this paper, we chose to follow the FAS approach.

The FAS (ν_1, ν_2) multigrid cycle starts at the target (finest) grid and, at each grid, it performs ν_1 distributed relaxation iterations before transferring residuals and solution approximation to the next coarse-grid that has doubled mesh sizes in each spatial direction. The coarse-grid is constructed in such a way that each coarse cell agglomerates eight fine-grid cells. All restriction operators, for residuals and for solutions, are linear operators with minimal symmetric stencils. Details of the inter-grid transfers used by the outer multigrid cycle are shown in the Appendix B. The formulation on the current grid is formed according to the standard FAS procedure [14–16]. The coarsening is continued recursively until the coarsest (usually 9^3) grid is reached and the coarsest-grid formulation is solved to (almost) zero residuals. The correction, defined as the difference between the final and the initial solution on the current grid, is then tri-linearly interpolated to the finer grid. On each grid, the obtained coarse-grid correction is added to improve the current solution approximation and followed by ν_2 relaxation iterations. Prolongation of the coarse-grid correction is continued to finer grids until the target grid approximation is corrected and relaxed. In the current version of the algorithm $\nu_1 = \nu_2 = 1$.

5.2. Distributed relaxation

5.2.1. Principal linearization

A basic step in developing an efficient multigrid algorithm is design of an efficient relaxation procedure. For nonlinear problems, the relaxation procedures are derived through Newton iterations recipe. The full Newton linearization of the Navier–Stokes equations (3) is a complicated operator, and its solution (inversion) involves a significant cost. To reduce the computational cost without compromising efficiency, one can opt to relaxation of a principal linearization. The principal linearization of a scalar equation contains the linearization terms that make major contributions to the residual per unit change in an unknown variable. The prin-

cipal terms thus generally depend on parameters of the problem, in particular, on the scale, or mesh size, of interest. For example, the discretized highest derivative terms are principal on grids with small enough mesh size. For a discretized system of differential equations, the principal terms are those contributing to the principal terms of the system determinant. Examples of principal linearization matrices for various flow equations are discussed elsewhere [17,18].

The relaxation scheme is defined for the equation

$$\mathbf{L}\delta\mathbf{q} = R(\mathbf{q}^n), \tag{19}$$

where $\mathbf{L}$ is a principal linearization matrix, $R(\mathbf{q}^n)$ is the residual of the nonlinear equations computed for the current approximate solution $\mathbf{q}^n$, and $\delta\mathbf{q} \equiv \mathbf{q}^{n+1} - \mathbf{q}^n$ is the correction computed in the relaxation.

Although significantly simplified by retaining only principal terms, the system (19) is still a set of complicated coupled equations. Therefore, a straightforward (*e.g.*, collective Gauss–Seidel) relaxation of $\mathbf{L}$ is not often effective. The distributed relaxation method replaces $\delta\mathbf{q}$ in (19) by $\mathbf{M}\delta\mathbf{w}$.

$$\mathbf{L}\mathbf{M}\delta\mathbf{w} = R(\mathbf{q}^n). \tag{20}$$

With an appropriate choice of the distribution matrix $\mathbf{M}$, the resulting matrix $\mathbf{LM}$ becomes lower triangular. The diagonal elements of $\mathbf{LM}$ are composed ideally of the separable factors of the matrix $\mathbf{L}$ determinant. These factors are discretization of scalar differential operators, so their efficient relaxation is a much simpler task than relaxing the entire system associated with $\mathbf{L}$. In relaxing scalar factors, any change introduced in the variables $\delta\mathbf{w}$ during relaxation is distributed, with the pattern defined by the matrix $\mathbf{M}$, to the primitive variables, $\delta\mathbf{q} = \mathbf{M}\delta\mathbf{w}$. Often, the variables $\delta\mathbf{w}$ need not to be stored (thereby, they termed sometimes as "ghost" variables); the changes introduced to $\delta\mathbf{w}$ are immediately distributed to the "true" correction variables $\delta\mathbf{q}$. In the solver reported in this paper, we do not take advantage of this option and solve for $\delta\mathbf{w}$ before distributing correction to $\delta\mathbf{q}$.

For nonlinear equations (18), the principal linearization matrix derived from the linearization around the current solution approximation is obtained as

$$\mathbf{L} = \begin{bmatrix} Q^h_{\bar{\nu}} - \frac{\hat{\lambda}}{\bar{\rho}}\partial^h_{xx} & -\frac{\hat{\lambda}}{\bar{\rho}}\partial^h_{xy} & -\frac{\hat{\lambda}}{\bar{\rho}}\partial^h_{xz} & \frac{1}{\rho}\partial^h_x & 0 \\ -\frac{\hat{\lambda}}{\bar{\rho}}\partial^h_{xy} & Q^h_{\bar{\nu}} - \frac{\hat{\lambda}}{\bar{\rho}}\partial^h_{yy} & -\frac{\hat{\lambda}}{\bar{\rho}}\partial^h_{yz} & \frac{1}{\rho}\partial^h_y & 0 \\ -\frac{\hat{\lambda}}{\bar{\rho}}\partial^h_{xz} & -\frac{\hat{\lambda}}{\bar{\rho}}\partial^h_{yz} & Q^h_{\bar{\nu}} - \frac{\hat{\lambda}}{\bar{\rho}}\partial^h_{zz} & \frac{1}{\rho}\partial^h_z & 0 \\ \gamma p\partial^h_x & \gamma p\partial^h_y & \gamma p\partial^h_z & Q^h & (1-\gamma)\kappa\Delta^h \\ (\gamma-1)\epsilon\partial^h_x & (\gamma-1)\epsilon\partial^h_y & (\gamma-1)\epsilon\partial^h_z & 0 & Q^h_\chi \end{bmatrix}, \tag{21}$$

where the discrete operator $Q^h_{\bar{\nu}} = \frac{3}{2h_t} - \bar{\nu}\Delta^h$, $\bar{\nu} := \mu/\bar{\rho}$, and Q^h_χ is similarly defined with $\chi := \kappa/\rho$. All the coefficients are computed from the current solution approximation and frozen during the course of relaxation. Thus

$$\det\mathbf{L} = (Q^h_{\bar{\nu}})^2[A_2(\Delta^h)^2 + A_1\Delta^h + A_0], \tag{22}$$

where coefficients A_i are defined as

$$\begin{aligned} A_0 &= (Q^h)^3, \\ A_1 &= -\frac{Q^h}{\rho}(Q^h(\kappa + \hat{\lambda} + \mu) + \rho c_s^2), \\ A_2 &= \frac{\kappa}{\rho^2}\left(Q^h(\hat{\lambda} + \mu) + \frac{\rho c_s^2}{\gamma}\right) \end{aligned} \tag{23}$$

and $Q^h = Q^h_0 = \frac{3}{2h_t}$ is a scalar factor, not a difference operator.

The determinant (22) can be further factorized

$$\det\mathbf{L} = (Q^h_{\bar{\nu}})^2 A_2(\Delta^h - X_1)(\Delta^h - X_2), \tag{24}$$

where $X_{1,2} = \frac{-A_1 \pm \sqrt{A_1^2 - 4A_0A_2}}{2A_2}$ are non-negative scalar factors within the physical range of parameters and solutions. The validity of the principal linearization (21) for the pressure and energy equations, Eqs. (10d) and

(10e), relies on the assumption that the dissipation function Φ (11) is negligible relative to other terms involving velocity gradient in these equations. Because $\Phi \sim \mu\|\nabla \boldsymbol{u}\|^2$, the condition $\Phi \ll \rho c_s^2 \|\nabla \boldsymbol{u}\|$ means $\mu\|\nabla \boldsymbol{u}\| \ll \gamma p$, or equivalently

$$\|\nabla' \boldsymbol{u}'\| Ma^2 \ll Re, \tag{25}$$

where $Re := \rho UL/\mu$, $Ma := U/c_s$, $\|\nabla' \boldsymbol{u}'\| := L\|\nabla \boldsymbol{u}\|/U$, and L and U are characteristic length and velocity, respectively. Therefore, so long as the condition (25) is satisfied, regardless the actual value of the Reynolds number Re, the principal linearization (21) is valid. Obviously, this condition is satisfied for smooth Newtonian flows. However, it can be violated for non-smooth flows, which have discontinuities and $\mu\|\nabla \boldsymbol{u}\|_{\max} = \mathrm{O}(1)$, hence Φ is no longer negligible. Consequently the principal linearization of the pressure and energy equations must include contributions from Φ for non-smooth flows.

5.2.2. Distribution matrix

The distribution matrix $\mathbf{M}$ is given by

$$\mathbf{M} = \begin{bmatrix} 1 & 0 & 0 & -\frac{1}{\rho}\partial_x^h Q_\chi^h & -\frac{(\gamma-1)\kappa}{\rho}\partial_x^h \Delta^h \\ 0 & 1 & 0 & -\frac{1}{\rho}\partial_y^h Q_\chi^h & -\frac{(\gamma-1)\kappa}{\rho}\partial_y^h \Delta^h \\ 0 & 0 & 1 & -\frac{1}{\rho}\partial_z^h Q_\chi^h & -\frac{(\gamma-1)\kappa}{\rho}\partial_z^h \Delta^h \\ \hat{\lambda}\partial_x^h & \hat{\lambda}\partial_y^h & \hat{\lambda}\partial_z^h & Q_\xi^h Q_\chi^h & Q_\xi^h(\gamma-1)\kappa\Delta^h \\ 0 & 0 & 0 & \frac{c_s^2}{\gamma\rho}\Delta^h & Q^h Q_\xi^h - c_s^2\Delta^h \end{bmatrix} \tag{26}$$

where $\breve{\xi} := (\hat{\lambda}+\mu)/\rho$, consequently,

$$\mathbf{LM} = \begin{bmatrix} Q_{\breve{v}}^h & 0 & 0 & 0 & 0 \\ 0 & Q_{\breve{v}}^h & 0 & 0 & 0 \\ 0 & 0 & Q_{\breve{v}}^h & 0 & 0 \\ \mathcal{P}\partial_x^h & \mathcal{P}\partial_y^h & \mathcal{P}\partial_z^h & A_2(\Delta^h - X_1)(\Delta^h - X_2) & 0 \\ \frac{c_s^2}{\gamma}\partial_x^h & \frac{c_s^2}{\gamma}\partial_y^h & \frac{c_s^2}{\gamma}\partial_z^h & 0 & A_2(\Delta^h - X_1)(\Delta^h - X_2) \end{bmatrix}, \tag{27}$$

where $\mathcal{P} \equiv \rho c_s^2 + \hat{\lambda} Q^h$. Thus, relaxation of the system (19) is reduced to relaxation of scalar factors located on the main diagonal of (27).

5.2.3. Inner multigrid cycle for scalar factors

The last two scalar factors appearing on the main diagonal of (27) approximate a fourth-order differential operator that is a composition of two second-order differential operators. Developing a suitable relaxation for such a composition is not straightforward; efficient relaxation schemes for the second-order operators are much easier to derive. Thus, an efficient procedure for relaxing the fourth-order operator

$$A_2(\Delta^h - X_1)(\Delta^h - X_2)\delta w = f \tag{28}$$

consists of two steps: first, one "inner" multigrid cycle is applied to the equation

$$(\Delta^h - X_1)\phi = f/A_2 \tag{29}$$

with initial approximation $\phi = (\Delta^h - X_2)\delta w$, which is typically zero because δw is a distributed correction. Then, one "inner" multigrid cycle is applied to the equation

$$(\Delta^h - X_2)\delta w = \phi. \tag{30}$$

To unify the treatment of all scalar factors, one inner multigrid cycle is applied to all factors on the main diagonal of (27), not only to the last two operators. The additional complexity related to employing a multigrid cycle instead of a single-grid relaxation is very small: complexity of the scalar operators is almost negligible comparing to complexity of the target nonlinear system; also, the 3D multigrid adds only a small fraction

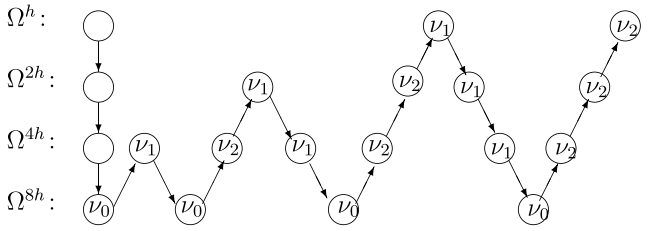

Fig. 5. Schematic of the FV-cycle for 4-level multigrid where v_0 denotes the number of relaxations on the coarsest mesh (Ω^{8h}).

to the work performed in relaxation on the finest grid because the complexity of each next coarse-grid is eight times smaller than the complexity of the previous fine-grid.

The relaxation scheme used for the inner cycle is the red–black relaxation. In the limiting case of $h_t \gg h$ when Q^h approaches zero together with X_1 and X_2, this relaxation provides smoothing factor of 0.445 [14], which becomes even better for larger values of X_1 and X_2 because of increased diagonal dominance of the discrete equations.

Some terms of the distribution matrix (26) are approximations to fourth-order differential operators. The high-order derivatives in the distribution matrix increase sensitivity of the correction $\delta\mathbf{q}$ to high-frequency error that can be introduced to $\delta\mathbf{w}$. In particular, if the initial error is very smooth (no high-frequency error components), red–black relaxation is known to generate some spurious high-frequency errors of a small amplitude depending on the amplitude and the frequency of the initial error. Appendix C contains the Fourier mode analysis explaining the generation of spurious high-frequency errors in red–black relaxation.

Even a small spurious high-frequency error can lead to significant initial increase in algebraic errors that can destroy TME or even provoke divergence of outer nonlinear iterations. To minimize spurious high-frequency errors, we employ the FV(v_1, v_2) multigrid cycle (a version of the F-cycle, sketched in Fig. 5), which dramatically reduces the amplitude of the smooth initial error. Note that a similar algorithm was used in [29].

The FV(2, 2) cycle is designed to implement preliminary reduction of smooth-error components and is used in our algorithm for inner multigrid. Convergence rates of inner multigrid cycles are always better than one order of magnitude per cycle.

6. Numerical results

The first series of tests illustrates the residual and the algebraic error convergence rates demonstrated by the outer multigrid cycle. Recall that the algebraic errors are measured as the difference between the solutions obtained after each cycle and the exact discrete solution corresponding to the zero residuals. The tests are performed for the initial approximation and the forcing terms defined by the exact analytical solution (17). The target spatial resolution of 129^3 is defined on the cube with the characteristic length of $L = 1$, i.e., the spatial mesh size $h = 1/128$ and the time step $h_t = 20$ h. The acoustic CFL number is CFL ≈ 60; the corresponding convective CFL number is $\mathrm{CFL_c} \approx 20$. The convergence of the outer FAS(1, 1) cycle is observed at the time level $T = 1.5625$. The initial approximation is obtained from the previous-time-level. The departure and transition points of the semi-Lagrangian discretization are updated after each cycle. Convergence of the L_∞ norm of the algebraic errors and the residuals of the implicit equations is shown in Fig. 6. The convergence is very fast exhibiting rates that are uniformly better than an order of magnitude per cycle and do not deteriorate for multiple iterations. The convergence rates remain the same for refined grids and larger CFL numbers.

The TME version of this algorithm applies only one outer multigrid cycle at each time level, before proceeding to the next time level. The solutions computed on grids with $h = 1/64, h_t = 10$ h and on grids with $h = 1/128, h_t = 20$ h. Fig. 7 shows the time evolution of the ratio of the L_∞ norms of algebraic and discretization errors for the u-velocity component and for the pressure. The ratios computed on the tested grids are almost identical, which indicates that the main error contribution is caused by time integration. On both grids at any time level, the ratios are well smaller than 1, which confirms the desired accuracy of the solution and shows that the efficiency of the algorithm is not degraded on finer grids and for larger CFL numbers. The estimated complexity of this solver is about seven minimal work units.

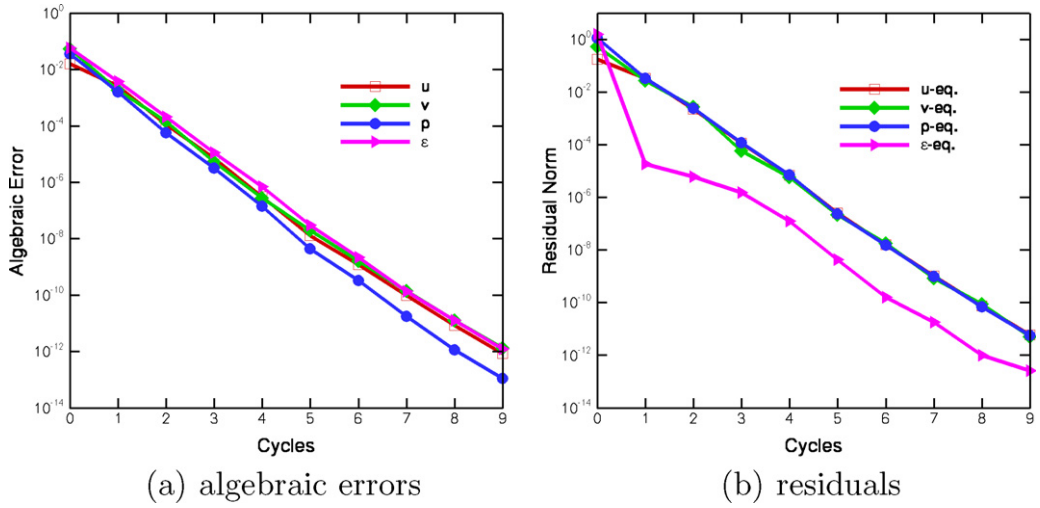

Fig. 6. Multigrid convergence of L_∞ norms of algebraic errors and residuals.

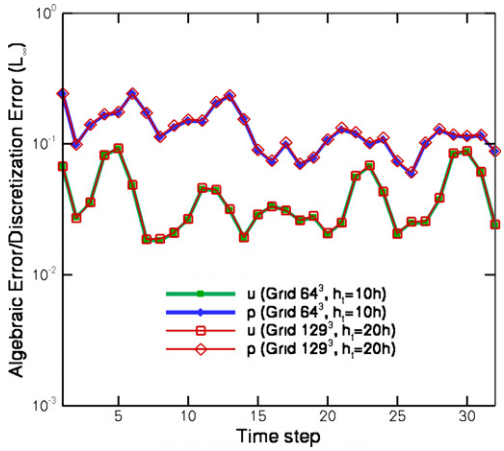

Fig. 7. The ratio of algebraic errors and discretization errors with only one cycle at each time step in the unsteady case.

In the current study, we directly measured the total complexity of the algorithm using the minimal work units, where one minimal work unit is the operation count in one residual evaluation performed in the time/space domain. A numerical test based on a 65^3 grid has been done on a 2.2 GHz AMD Opteron processor. Evaluation of spatial residuals at a hundred time levels took 150 s, while the total time for one hundred time level evolutions with one outer multigrid cycle at each level was 1352 s. Thus, the wall-clock time to obtain solution with discretization accuracy was approximately the same as for nine residual evaluations in the time–space domain. The numerically verified complexity of the solver is just a little larger than the predicted complexity of seven minimal work units. Note that the time test was performed with a research version of the code (performing some unnecessary computations) and with no optimization whatsoever. With minimal optimization efforts, the theoretical and numerically verified complexity estimates are expected to match.

Finally, we conduct a DNS of decaying homogeneous isotropic turbulence (DHIT) with the current TME method. DHIT is a classic problem for turbulence research. In this case, the simulation is conducted in a three-dimensional cube with periodic boundary conditions. One only needs to specify a random isotropic initial velocity field. In the current study, we consider a weak compressible flow with a low Mach number $Ma = 0.2$. The initial velocity field is generated in the spectral space $\boldsymbol{k}$ specified by the initial energy spectrum with random phase as the following [30,13]:

$$\widetilde{E}(\boldsymbol{k},0)=\begin{cases}0.038k^{m}\mathrm{e}^{-0.14k^2}, & k\in[k_{\min},k_{\max}],\\ 0, & k\notin[k_{\min},k_{\max}],\end{cases} \tag{31}$$

where $\widetilde{E}(\boldsymbol{k},0)$ is the initial energy spectrum and $k=\|\boldsymbol{k}\|$ is the wave-number. Then the initial velocity field is transferred to physical space. The initial density $\rho(\boldsymbol{x},t=0)$ consistent with the initial velocity field $\boldsymbol{u}(\boldsymbol{x},t=0)$ is obtained by an iteration procedure [31].

The energy spectrum is governed by the following equation [13]:

$$\partial_t\widetilde{E}(\boldsymbol{k},t)=-\widetilde{T}(\boldsymbol{k},t)-2\nu k^2\widetilde{E}(\boldsymbol{k},t), \tag{32}$$

where $\widetilde{T}(\boldsymbol{k},t)$ represents the nonlinear energy transfer between modes [13]. The kinetic energy $K(t)$ and dissipation $\varepsilon(t)$ are given by

$$K(t)=\int\widetilde{E}(\boldsymbol{k},t)\,\mathrm{d}\boldsymbol{k},\quad \varepsilon(t)=2\nu\int k^2\widetilde{E}(\boldsymbol{k},t)\,\mathrm{d}\boldsymbol{k}. \tag{33}$$

The isotropic turbulence can be characterized by the transverse Taylor-microscopic Reynolds number

$$Re_\lambda=\frac{u_{\mathrm{rms}}\lambda}{\nu},\quad \lambda=\sqrt{\frac{15\nu u_{\mathrm{rms}}^2}{\varepsilon}}=\sqrt{\frac{10\nu K}{\varepsilon}}, \tag{34}$$

where $u_{\mathrm{rms}}=\sqrt{2K/3}$ is the root mean square (rms) of the velocity field and λ is the transverse Taylor-microscale length. It has been observed that the decay of kinetic energy K and dissipation rate ε follows the power law after the initial transient period time [13],

$$\frac{K(t)}{K_0}\sim\left(\frac{t}{t_0}\right)^{-n},\quad \frac{\varepsilon(t)}{\varepsilon_0}\sim\left(\frac{t}{t_0}\right)^{-(n+1)}, \tag{35}$$

where K_0 and ε_0 are the values of kinetic energy and dissipation rate at the reference time $t_0=nK_0/\varepsilon_0$.

In the present study, we choose $m=4$ in (31) for the initial field. Other parameters in the simulation are: $[k_{\min},k_{\max}]=[5,15]$, $u_{\mathrm{rms}}=0.0577$ and $\nu=6.9\times10^{-4}$, which results in the $Re_\lambda\approx31$. Our computation is performed in a cube with the characteristic length of $L=2\pi$ based on the grid size of 129^3. The evolutions of the normalized kinetic energy K/K_0 and dissipation rate $\varepsilon/\varepsilon_0$ with time are presented in Fig. 8(a). In the absence of the production, the kinetic energy K decays monotonically in time while the dissipation rate ε goes up at the early stage. This increase in dissipation rate is consistent with the known turbulence physics. Beyond this period, the dissipation rate also decays monotonically as well as the kinetic energy. Our results are in agreement with the existing ones [32–35].

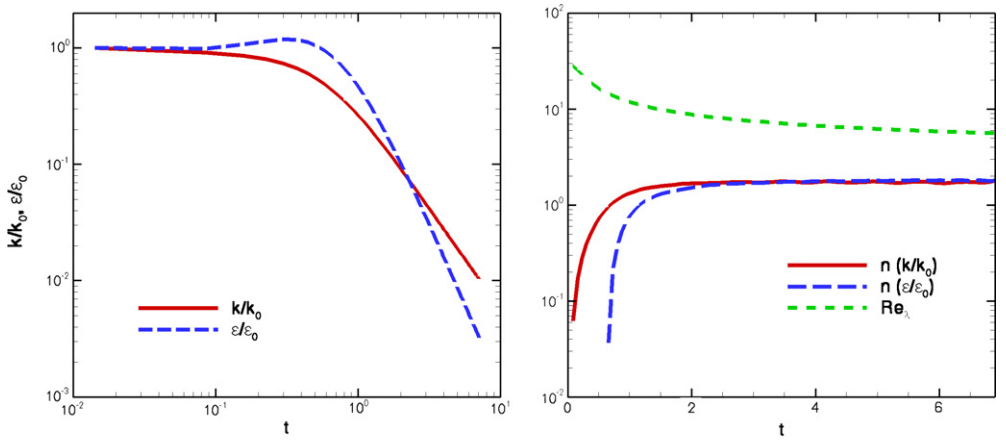

(a) $K(t)/K_0$ and $\varepsilon(t)/\varepsilon_0$ (b) $\mathrm{Re}_\lambda(t)$, $n_K(t)$ and $n_\epsilon(t)$

Fig. 8. DNS of decaying homogeneous isotropic turbulence in 3D by using the TME multigrid method: (a) the evolutions of the total kinetic energy $K(t)/K_0$ and the dissipation rate $\varepsilon(t)/\varepsilon_0$, and (b) the dynamics of the transverse Taylor-microscale Reynolds number $Re_\lambda(t)$, and decay exponents $n_K(t)$ and $n_\epsilon(t)$ computed from the energy $K(t)/K_0$ and the dissipation rate $\varepsilon(t)/\varepsilon_0$, respectively.

Fig. 8(b) shows the evolution of the decay exponent n in time computed from both the kinetic energy $K(t)$ and the dissipation rate ε. We can see that $n_K(t)$ and $n_\epsilon(t)$ converge to each other after a initial period of time about $t/t_0 \approx 2$. The decay of the kinetic energy K and the dissipation rate ε follows the power law with the decay exponent $n \approx 1.73$ after the initial transient period time. This value agrees well with previous results [32–35]. The evolution of Re_λ in time is also illustrated in Fig. 8(b), which shows that Re_λ is decreasing as the turbulence decays. Fig. 8(b) shows that the grid Reynolds number $Re^*_\lambda := Re_\lambda/N < 1.0$ for $N = 129$, indicating that the flow is well resolved.

7. Conclusions and future work

Textbook multigrid efficiency (TME) solver has been developed for three-dimensional compressible time-dependent Navier–Stokes equations discretized with an implicit, second-order accurate, unconditionally stable, and non-conservative scheme. A semi-Lagrangian approach has been used to discretize the time-dependent convection part of the equations. The viscous terms and the pressure gradient are discretized on a staggered-grid. Efficient distributed relaxation scheme with inner multigrid cycles has been developed. Accuracy, optimal convergence rates, and fast reduction of algebraic errors below the level of discretization accuracy have been demonstrated. The efficiency of the solver does not deteriorate for high Reynolds numbers and for large time steps. The TME solver has been applied to direct numerical simulations of decaying turbulence and the results agree with previous ones obtained by explicit solvers.

For the applications reported in this paper, the solver has been applied to a non-conservative formulation on a domain with periodic boundary conditions. Currently we are testing a version of the multigrid solver with general (inflow, outflow, and no-slip) boundary conditions. Semi-Lagrangian method is slightly modified near the boundaries, but retains its favorable properties, such as second-order accuracy and stability. The distributed relaxation applied in the interior is complimented with a block-relaxation near boundaries. We are also planing to test conservative formulations corresponding to the semi-Lagrangian methodology. Several such schemes have been developed and applied within environmental science community [36,37].

Acknowledgements

WL, YP and LSL would like to acknowledge the support from US Department of Defense under AFOSR-MURI Project "*Hypersonic Transition and Turbulence with Non-Equilibrium Thermochemistry*" (Program Manager: Dr. J. Schmisseur) and NASA through an NIA contract ODU-06-01. BD would like to acknowledge the support from NASA through the Contract NAS1-2117, Task Order NNL04AA96T "*Rotorcraft Aeromechanics*" (Technical Monitor: Dr. M.W. Nixon, Army Research Laboratory) and Contract NNL07AA31C "*Development of a Multidisciplinary Computational Tool for Accurate and Efficient Rotorcraft Noise Prediction*" (Technical Monitor: Dr. D.M. Nark), and US National Science Foundation under Grant DMS-0327560 "*Numerical Coarsening and Upscaling for Geophysical Fluid Dynamics*." The authors would also like to acknowledge the computing resources available to them at Department of Computer Science and Office of Computing and Communications Services, Old Dominion University.

Appendix A. Unconditional linear stability of semi-Lagrangian discretization

In this section, we present a von-Neumann stability analysis of a 1D constant-coefficient convection–diffusion equation

$$\partial_t u + a\partial_x u - \mu\partial_{xx} u = f, \tag{A.1}$$

in which the time-dependent convection term discretized on a uniform grid with a semi-Lagrangian method. Assuming $a > 0$, the discretization is given by

$$\frac{1}{h_t}\left\{\frac{3}{2}u_i^n - 2\left[(1-s)u_{i-k}^{n-1} + s u_{i-(k+1)}^{n-1}\right] + \frac{1}{2}\left[(1-s)u_{i-2k}^{n-2} + s u_{i-2(k+1)}^{n-2}\right]\right\} - \mu\frac{1}{h^2}\left(u_{i+1}^n - 2u_i^n + u_{i-1}^n\right) = f_i^n, \tag{A.2}$$

where h_t and h are the time step and the spatial mesh size, respectively, n and i are time and spatial indexes, respectively, and

$$\mathrm{CFL_c} \equiv \frac{ah_t}{h} = k + s, \tag{A.3}$$

where $\mathrm{CFL_c}$ is the convective CFL number (2) and $k = [\mathrm{CFL_c}]$ is the integer part of $\mathrm{CFL_c}$ and $0 \leqslant s < 1$.

For a solution in the form

$$u_i^n = \lambda^n \mathrm{e}^{\imath\omega}, \tag{A.4}$$

where $\imath := \sqrt{-1}$, the characteristic polynomial corresponding to the discretization (A.2) is

$$\left(\frac{3}{2} - \frac{2}{Re_L}(\cos\omega - 1)\right)\lambda^2 - 2\mathrm{e}^{-\imath k\omega}((1-s) + s\mathrm{e}^{-\imath\omega})\lambda + \frac{1}{2}\mathrm{e}^{-\imath 2k\omega}\left((1-s) + s\mathrm{e}^{-\imath 2\omega}\right) = 0, \tag{A.5}$$

the coefficients of the polynomial depend on three parameters: the spatial frequency, ω, the local Reynolds number, $Re_L = \frac{h^2}{\mu h_t}$, and the convective CFL number, $\mathrm{CFL_c}$. A simple check shows that for any ω and any positive Re_L and $\mathrm{CFL_c}$, the amplitudes of the roots of the characteristic polynomial (A.5) are bounded by one, which implies unconditional stability of the scheme (A.2).

Appendix B. Outer multigrid: inter-grid transfers

The version of the outer FAS multigrid cycle used in this solver constructs the coarse-grid cells by merging eight fine-grid cells. The obtained grids are not nested. Other coarse-grid constructions are also possible and are not expected to affect adversely the algorithm efficiency. All prolongation operators used in the multigrid cycle are tri-linear interpolation operators. In this appendix, we present explicit formulas for some of the restriction operators in use.

For definiteness, we assume a three-index integer numeration of cell centers on each grid and half-index shifts to indicate cell-faces centers. The numeration starts as $(i_x, i_y, i_z) = (1, 1, 1)$ at the left-back-bottom corner and increases dimension-by-dimension.

The restriction operator describing coarsening of the pressure and energy related quantities is an averaging over eight corresponding fine-grid quantities:

$$P^{\mathrm{c}}_{i_x,i_y,i_z} = \frac{1}{8}\sum_{l,m,n=0}^{1} p^{\mathrm{f}}_{2i_x-l,2i_y-m,2i_z-n}, \tag{B.1}$$

where $P^{\mathrm{c}}_{i_x,i_y,i_z}$ and $p^{\mathrm{f}}_{i_x,i_y,i_z}$ are the coarse and fine-grid values, respectively.

The restriction operator describing coarsening of the u-velocity related quantities is defined as

$$U^{\mathrm{c}}_{i_x+\frac{1}{2},i_y,i_z} = \frac{1}{16}\sum_{m,n=0}^{1}\left(u^{\mathrm{f}}_{2i_x-\frac{1}{2},2i_y-m,2i_z-n} + 2u^{\mathrm{f}}_{2i_x+\frac{1}{2},2i_y-m,2i_z-n} + u^{\mathrm{f}}_{2i_x+\frac{3}{2},2i_y-m,2i_z-n}\right). \tag{B.2}$$

Other velocity related restriction operators are analogously defined.

Appendix C. Fourier mode analysis of three-dimensional red–black relaxation

In this appendix, we apply the local mode Fourier (LMF) analysis for analyzing three-dimensional red–black relaxation of the standard seven-point discrete Laplacian. Foundations and applications of the LMF analysis can be found in the pioneering paper [22] and in textbooks, e.g., [14,38]. The Fourier symbol of the relaxation is an 8×8 block-diagonal matrix acting in the linear vector space corresponding to the amplitudes of the octet of the Fourier components, $\{\mathrm{e}^{\jmath[(\theta_x+l\pi)i_x+(\theta_y+m\pi)i_y+(\theta_z+n\pi)i_z]}\}$, $l, m, n = 0, 1$, with normalized Fourier frequencies $\bar{\theta} = (\theta_x, \theta_y, \theta_z)$ satisfying $\max(|\,\bar{\theta}\,|) := \max(|\,\theta_x\,|, |\,\theta_y\,|, |\,\theta_z\,|) \leqslant \pi$. Explicitly, for a pair of Fourier components

$$\bar{\mathbf{e}}(\bar{\theta}) = (\mathrm{e}^{\jmath(\theta_x i_x+\theta_y i_y+\theta_z i_z)}, \mathrm{e}^{\jmath[(\theta_x+\pi)i_x+(\theta_y+\pi)i_y+(\theta_z+\pi)i_z]}), \tag{C.1}$$

the symbol, $\mathbf{R}(\bar{\theta})$, of the red–black relaxation is defined as a parameterized matrix

$$\mathbf{R}(\bar{\theta}) = \begin{bmatrix} \frac{C(\bar{\theta})[1+C(\bar{\theta})]}{2} & \frac{C(\bar{\theta})[1+C(\bar{\theta})]}{2} \\ \frac{C(\bar{\theta})[1-C(\bar{\theta})]}{2} & \frac{C(\bar{\theta})[1-C(\bar{\theta})]}{2} \end{bmatrix}, \tag{C.2}$$

where $C(\bar{\theta}) = (\cos\theta_x + \cos\theta_y + \cos\theta_z)/2$. In particular, if the initial error is given as $\bar{\mathbf{e}}(\bar{\theta}) \cdot \bar{\mathbf{a}}^0$, where $\bar{\mathbf{a}}^0 = (a_1^0, a_2^0)^{\mathsf{T}}$ is the vector of amplitudes, then after the relaxation the new amplitudes, $\bar{\mathbf{a}}^1$, satisfy

$$\bar{\mathbf{a}}^1 = \mathbf{R}(\bar{\theta}) \cdot \bar{\mathbf{a}}^0. \tag{C.3}$$

Assuming that the initial error has no high-frequency content, and $a_1^0 = 1$, $a_2^0 = 0$, and $\max(|\bar{\theta}|) < \frac{\pi}{2}$, then the red–black relaxation yields a high-frequency error with the amplitude $a_2^1 = a_1^0 C(\bar{\theta})[1 - C(\bar{\theta})]/2$ corresponding to the Fourier mode $(\theta_x + \pi, \theta_y + \pi, \theta_z + \pi)$. Even though the amplitude of $a_2^1 \sim a_1^0 \mathrm{O}((\max(|\bar{\theta}|))^2) \sim \mathrm{O}(h^2)$ is second-order small compared to a_1^0, the high-frequency error a_2^1 is still amplified considerably by the distribution matrix by a factor of $\mathrm{O}(h^{-4})$. Therefore, an inner FV multigrid cycle must be used to guarantee a sufficiently small initial smooth-error amplitude.

References

[1] S. Sarkar, The stabilizing effect of compressibility in turbulent shear-flow, J. Fluid Mech. 282 (2000) 163–186.
[2] F. Jacobitz, S. Sarkar, A direct numerical study of transport and anisotropy in a stably stratified turbulent flow with uniform horizontal shear, Flow Turbul. Combust. 63 (1–4) (2000) 343–360.
[3] R. Samtaney, D.I. Pullin, B. Kosović, Direct numerical simulation of decaying compressible turbulence and shocklet statistics, Phys. Fluids 13 (5) (2001) 1415–1430.
[4] S.A. Stanley, S. Sarkar, J.P. Mellado, A study of the flow-field evolution and mixing in a planar turbulent jet using direct numerical simulation, J. Fluid Mech. 450 (2002) 377–407.
[5] S. Sarkar, The effect of stable stratification on turbulence anisotropy in uniformly sheared flow, Comput. Math. Appl. 46 (4) (2003) 639–646.
[6] H. Foysi, S. Sarkar, R. Friedrich, Compressibility effects and turbulence scalings in supersonic channel flow, J. Fluid Mech. 509 (2004) 207–216.
[7] M.P. Martín, G.V. Candler, A parallel implicit method for the direct numerical simulation of wall-bounded compressible turbulence, J. Comput. Phys. 215 (1) (2006) 153–171.
[8] E.M. Taylor, M.W. Wu, P. Martín, Optimization of nonlinear error for weighted essentially non-oscillatory methods in direct numerical simulations of compressible turbulence, J. Comput. Phys. 223 (1) (2006) 384–397.
[9] Y. Kaneda, T. Ishihara, M. Yokokawa, K. Itakura, A. Uno, Energy dissipation rate and energy spectrum in high resolution direct numerical simulations of turbulence in a periodic box, Phys. Fluids 15 (2) (2003) L21–L24.
[10] K. Yoshida, J. Yamaguchi, Y. Kaneda, Regeneration of small eddies by data assimilation in turbulence, Phys. Rev. Lett. 94 (1) (2005) 014501.
[11] T. Ishida, P.A. Davidson, Y. Kaneda, On the decay of isotropic turbulence, J. Fluid Mech. 564 (2006) 455–475.
[12] Y. Kaneda, T. Ishihara, High-resolution direct numerical simulation of turbulence, J. Turbul. 7 (20) (2006) 1–17.
[13] S.B. Pope, Turbulence Flows, Cambridge University Press, Cambridge, UK, 2000.
[14] U. Trottenberg, C.W. Oosterlee, A. Schüler, Multigrid, Academic Press, London, 2000.
[15] A. Brandt, Multigrid techniques: 1984 guide with applications to fluid dynamics, in: Lecture Notes for the Computational Fluid Dynamics, Lecture Series of the Von Karman Institute for Fluid Dynamics, The Weizmann Institute of Science, Rehovot, Israel, 1984.
[16] A. Brandt, Guide to multigrid development, in: W. Hackbusch, U. Trottenberg (Eds.), Multigrid Methods, Lecture Notes in Mathematics, vol. 960, Springer, Berlin, 1982.
[17] A. Brandt, B. Diskin, J.L. Thomas, Textbook multigrid efficiency for computational fluid dynamics simulations. AIAA paper 2001-2570, AIAA, June 2001.
[18] J.L. Thomas, B. Diskin, A. Brandt, Textbook multigrid efficiency for fluid simulations, Annu. Rev. Fluid Mech. 35 (2003) 317–340.
[19] P. Wesseling, C.W. Oosterlee, Geometric multigrid with applications to computational fluid dynamics, J. Comput. Appl. Math. 128 (2001) 311–334.
[20] G. Wittum, Multi-grid methods for Stokes and Navier–Stokes equations with transforming smoothers: algorithms and numerical results, Numer. Math. 54 (1989) 543–563.
[21] A. Brandt, Appendic C: Recent developments in multigrid efficiency in computational fluid dynamics, pp. 573–589. In [14], 2000.
[22] A. Brandt, Multi-level adaptive solutions to boundary value problems, Math. Comput. 31 (1977) 333–390.
[23] W.L. Briggs, S.F. McCormick, V.E. Henson, Multigrid Tutorial, second ed., SIAM Publications, Philadelphia, USA, 2000.
[24] A. Brandt, N. Dinar, Multigrid solutions to flow problems, in: S. Perter (Ed.), Numerical Methods for Partial Differential Equations, Academic Press, New York, 1979, pp. 53–147.
[25] A. Brandt, I. Yavneh, On multigrid solution of high-Reynolds incompressible entering flow, J. Comput. Phys. 101 (1992) 151–164.

[26] D. Xiu, G.E. Karniadakis, A semi-Lagrangian high-order method for Navier–Stokes equations, J. Comput. Phys. 172 (2001) 658–684.
[27] D. Mavriplis, An assessment of linear versus nonlinear multigrid methods for unstructured grid solvers, J. Comput. Phys. 175 (1) (2002) 302–325.
[28] I. Yavneh, G. Dardyk, A multilevel nonlinear method, SIAM J. Sci. Comput. 28 (1) (2006) 24–46.
[29] A. Brandt, J. Greenwald, Parabolic multigrid revisited, in: W. Hackbusch, U. Trottenberg (Eds.), Multigrid Methods, vol. III, Birkhäuser, Basel, 1991, pp. 143–154.
[30] T. Miyauchi, T. Ishizu, Direct numerical simulation of homogeneous isotropic turbulence – decay of passive scalar fluctuation. JSME Preprint No. 914-2, 1991.
[31] R. Mei, L.-S. Luo, P. Lallemand, D. d'Humières, Consistent initial conditions for lattice Boltzmann simulations, Comput. Fluids 35 (8/9) (2006) 855–862.
[32] N.N. Mansour, A.A. Wray, Decay of isotropic turbulence at low Reynolds number, Phys. Fluids 6 (1994) 808–814.
[33] M.-J. Huang, A. Leonard, Power-law decay of homogeneous turbulence at low Reynolds numbers, Phys. Fluids 6 (1994) 3765–3775.
[34] H. Yu, S.S. Girimaji, L.-S. Luo, Lattice Boltzmann simulations of decaying homogeneous isotropic turbulence, Phys. Rev. E 71 (2005) 016708.
[35] H. Yu, S.S. Girimaji, L.-S. Luo, DNS and LES of decaying isotropic turbulence with and without frame rotation using lattice Boltzmann method, J. Comput. Phys. 209 (2) (2005) 599–616.
[36] S.G. Wallis, The numerical solution of the advection–dispersion equation: a review of some basic principles, Acta Geophys. 55 (1) (2007) 85–94.
[37] S.G. Wallis, J.R. Manson, L. Filippi, A conservative semi-Lagrangian algorithm for one-dimensional advection–diffusion, Commun. Numer. Meth. Eng. 14 (1) (1998) 671–679.
[38] R. Wienands, W. Joppich, Practical Fourier Analysis for Multigrid Methods, Chappman & Hall, Boca Raton, FL, 2005.